



Two-point Separation Functions for Modeling Wide Binary Systems in Nearby Dwarf Galaxies

Christopher Kervick¹ , Matthew G. Walker¹ , Jorge Peñarrubia^{2,3}, and Sergey E. Koposov^{2,4} ¹ McWilliams Center for Cosmology, Dept. of Physics, Carnegie Mellon University, 5000 Forbes Avenue, Pittsburgh, PA 15213, USA; ckervick@andrew.cmu.edu² Institute for Astronomy, University of Edinburgh, Royal Observatory, Blackford Hill, Edinburgh EH9 3HJ, UK³ Center for Statistics, University of Edinburgh, School of Mathematics, Edinburgh, EH9 3FD, UK⁴ Institute of Astronomy, University of Cambridge, Madingley Road, Cambridge CB3 0HA, UK

Received 2021 July 15; revised 2022 February 28; accepted 2022 March 3; published 2022 April 14

Abstract

We use a geometric method to derive (two-dimensional) separation functions among pairs of objects within populations of specified position function dN/dR . We present analytic solutions for separation functions corresponding to a uniform surface density within a circular field, a Plummer sphere (viewed in projection), and the mixture thereof—including contributions from binary objects within both subpopulations. These results enable inferences about binary object populations via direct modeling of object position and pair separation data, without resorting to standard estimators of the two-point correlation function. Analyzing mock data sets designed to mimic known dwarf spheroidal galaxies, we demonstrate the ability to recover input properties including the number of wide binary star systems and, in cases where the number of resolved binary pairs is assumed to be \gtrsim a few hundred, characteristic features (e.g., steepening and/or truncation) of their separation function. Combined with forthcoming observational capabilities, this methodology opens a window onto the formation and/or survival of wide binary populations in dwarf galaxies, and offers a novel probe of inferred dark matter substructure on the smallest galactic scales.

Unified Astronomy Thesaurus concepts: Dwarf galaxies (416); Dark matter (353); Binary stars (154); Stellar populations (1622)

1. Introduction

Wide binary star systems are vulnerable to disruption via encounters with perturbers (e.g., Chandrasekhar 1944; Heggie 1975; Weinberg et al. 1987; Jiang & Tremaine 2010), making them useful tracers of dark structure (e.g., Bahcall et al. 1985; Chanamé & Gould 2004; Yoo et al. 2004). Usually detected as stellar pairs with common proper motion, Galactic wide binaries with separations $2 \lesssim \log_{10}(s/\text{A.U.}) \lesssim 4$ are typically characterized using a power-law separation function, $p(s) \propto s^{-\gamma}$, with $\gamma \approx 1.0 - 1.6$ (Chanamé & Gould 2004; Lépine & Bongiorno 2007; Andrews et al. 2017; El-Badry & Rix 2018). At larger separations, the power-law slope appears to steepen by an amount that depends on age and kinematics (Tian et al. 2019). Characterization of the binary separation function in different environments is crucial for understanding the formation and destruction of these weakly bound systems (Kouwenhoven et al. 2010; Moeckel & Bate 2010; El-Badry & Rix 2018; Peñarrubia 2021).

Wide binaries within the Milky Way's nearest satellites can potentially trace low-mass dark matter halo structure and substructure. The faintest dwarf galaxies have the highest dynamical mass-to-light ratios and inferred dark matter densities known, with $M/L_V \sim 10^{2-4}$ in solar units and $\rho \gtrsim 1 M_\odot \text{pc}^{-3}$ within their half-light radii (Mateo 1998; McConnachie 2012; Simon 2019). In the scale-free hierarchy of structure expected under the cold dark matter paradigm, such high dark matter densities imply that of all galaxies, the faintest dwarfs host the highest number densities of subhalo (and sub-subhalo, etc.)

perturbers (e.g., Springel et al. 2008). Indeed, N -body experiments demonstrate that on ultrafaint dwarf galaxy scales, the wide binary separation function is strongly sensitive to both the structure and amount of substructure within the host dark matter halo (Peñarrubia et al. 2010, 2016).

It is already well known that the Milky Way's faint satellites contain significant numbers of short-period binary stars ($P \lesssim 100$ yr). Several multi-epoch spectroscopic studies have identified likely binary systems as radial velocity variables with amplitudes up to $\sim 10 \text{ km s}^{-1}$, implying binary fractions of $f_b \approx 0.5$ (Koposov et al. 2011; Martinez et al. 2011; Minor 2013; Koch et al. 2014; Spencer et al. 2018). Similar fractions are derived from deep Hubble Space Telescope imaging of several ultrafaint dwarf galaxies based on the tendency of unresolved pairs to broaden the main sequence redward and brighter (Geha et al. 2013). However, these techniques necessarily miss wide binaries, which can have orbital periods exceeding thousands of years and may be resolved as point-source pairs. Furthermore, finding wide binaries via common proper motions at dwarf galaxy distances ($\sim 20-100$ kpc) would require precision $\lesssim 1$ milliarcsecond century⁻¹ at ~ 20 th magnitude, two orders of magnitude finer than what is delivered by Gaia's EDR3 catalog (Gaia Collaboration et al. 2021). Thus empirical constraints on wide binary populations within dwarf galaxies are at present nonexistent.

As a result, we do not know how or even whether wide binaries ever form within dwarf galaxies, much less how or whether they survive. Possible formation mechanisms include the same mechanisms as are invoked to explain wide binaries observed within the galaxy, e.g., (1) gravitational entrapment of neighbors as star-forming regions expand in response either to rapid gas loss (Kouwenhoven et al. 2010; Moeckel & Bate 2010) or to collisional relaxation (Moeckel & Clarke 2011), (2) three-body interactions in which one star is

scattered to a large orbit, but remains weakly bound to a relatively compact pair (Reipurth & Mikkola 2012), (3) binding of adjacent prestellar cores that move at slow relative velocity within the star-forming cloud (Tokovinin 2017), and/or (4) entrapment within the long-lived tails that emanate from tidally disrupted star clusters (Peñarrubia 2021).

Of course, the only way to prove that wide binaries both form and survive within dwarf galaxies would be to find them. Here we investigate the detectability of wide binaries in dwarf galaxies via single-epoch images that might resolve binary pairs. For reference, at a distance of 100 kpc, a pair of objects separated by 0.1 pc subtends $0''.2$ —approximately four times the diffraction limit of the Hubble Space Telescope and the upcoming Nancy Grace Roman Space Telescope.

The workhorse statistic for analyzing spatial inhomogeneities is the two-point correlation function (2PCF; e.g., Peebles 1980), which characterizes object clustering as a function of spatial scale. Specifically, the 2PCF quantifies the “excess” number of object pairs at a given separation with respect to the expectation for a random field. The 2PCF is widely used, e.g., to infer cosmological parameters from observations of large-scale structure (e.g., DES Collaboration et al. 2021). More relevant to the present study, Longhitano & Binggeli (2010) model the 2PCF of late-type stars in the solar neighborhood, reporting that $\sim 10\%$ of such stars belong to wide binary systems with projected separation $10^{-3} \lesssim s/(\text{pc}) \lesssim 1$.

Standard estimators of the 2PCF from cosmological large-scale structure quantify the expected “background” by averaging over large numbers of Monte Carlo realizations of the random field (e.g., Davis & Peebles 1983; Hamilton 1993; Landy & Szalay 1993). This procedure can faithfully account for features in the 2PCF that arise due to complications such as survey footprint, incompleteness, and known selection effects.

For the purpose of studying wide binary stars in dwarf galaxies, here we take a different approach that exploits the relative simplicity of these systems. For nearby dwarf galaxies, the random field of resolved stars is generally well characterized by an analytic surface number density function that includes an approximately uniform foreground (Milky Way) component (e.g., Irwin & Hatzidimitriou 1995; Martin et al. 2008; Moskowicz & Walker 2020). Here we develop a formalism for calculating two-point separation functions directly from the surface number density function—including the contribution from binary objects. We derive analytic results for the case in which the number density function is the mixture of a Plummer sphere and a uniform background—the scenario commonly invoked to model dwarf galaxy star counts. While these results can provide random-field input to a standard 2PCF estimator, they also provide a means to infer properties of binary object populations via direct modeling of the empirical separation function. We demonstrate the latter capability using mock imaging catalogs generated to mimic structural parameters observed for the Milky Way’s known dwarf-galactic satellites, highlighting the conditions under which wide binary populations—if they exist—can reliably be detected and characterized within these systems.

2. 2D Separation Functions

First we develop a formalism for calculating 2D separation functions. Consider a population of objects whose 2D (projected onto the plane of the sky) positions, $\mathbf{R} \in \mathbb{R}^2$, are

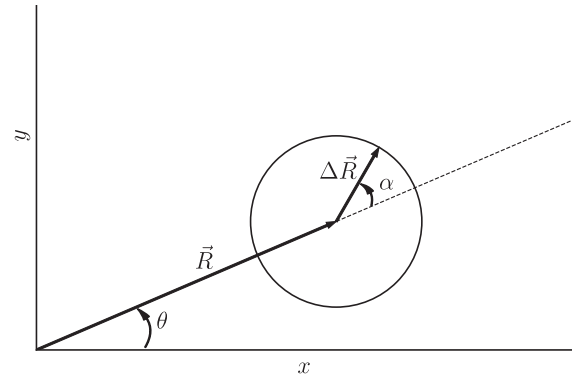


Figure 1. Geometry for calculating the probability density for separations of objects from position \mathbf{R} (see Equation (1)).

distributed randomly, via a Poisson point process, according to the surface number density function $\Sigma(\mathbf{R}) \equiv dN/d\mathbf{R}$. The total number of objects has the expectation value $\langle N \rangle = \iint \Sigma(\mathbf{R}) d\mathbf{R}$. The probability density of the object positions is then $p(\mathbf{R}) = \Sigma(\mathbf{R})/\langle N \rangle$. We seek to calculate the probability density for separations between pairs of objects drawn randomly from the population.

Figure 1 illustrates the relevant geometry. Letting α be the angle between \mathbf{R} and the vector displacement to a second position $\mathbf{R} + \Delta\mathbf{R}$, the number of objects that are separated from \mathbf{R} by projected distance within the interval $s, s + ds$ is $\mu(s|\mathbf{R})ds$, where

$$\mu(s|\mathbf{R}) \equiv \frac{dN}{ds} \Big|_{\mathbf{R}} = \int_0^{2\pi} \Sigma(\mathbf{R} + \Delta\mathbf{R}) s d\alpha, \quad (1)$$

is the conditional separation function, $\Delta\mathbf{R} = s(\cos(\theta + \alpha)\hat{x} + \sin(\theta + \alpha)\hat{y})$, and θ is the position angle at \mathbf{R} . The number of pairs having one object within the position interval $\mathbf{R}, \mathbf{R} + d\mathbf{R}$ and a separation within the interval $s, s + ds$ is $\psi(s, \mathbf{R})ds d\mathbf{R}$, where

$$\psi(s, \mathbf{R}) \equiv \frac{dN}{d\mathbf{R} ds} = \Sigma(\mathbf{R}) \mu(s|\mathbf{R}) \quad (2)$$

is the joint position-separation function. The number of pairs having a separation within the interval $s, s + ds$, regardless of position, is $\phi(s)ds$, where

$$\phi(s) \equiv \frac{dN}{ds} = \iint \psi(s, \mathbf{R}) d\mathbf{R} \quad (3)$$

is the marginal separation function.

For the purpose of calculating normalized probability densities, these separation functions integrate to $\int \mu(s|\mathbf{R})ds = \langle N \rangle$ and $\iint \psi(s, \mathbf{R})ds d\mathbf{R} = \int \phi(s)ds = \langle N \rangle^2$.

We note that $\phi(s)$ is equivalent to the derivative of Ripley’s K-function, which is defined in terms of spatial point processes (Baddeley et al. 2016). Our novel derivation, however, allows a direct calculation of the separation functions and, as we show below (Section 2.2), can straightforwardly include contributions from the splitting of some objects into pairs of binary companions whose internal separations are independent of $\Sigma(\vec{R})$.

2.1. Mixtures

It is useful to generalize to the case in which the population of objects comprises a mixture of N_{pop} distinct subpopulations that each independently follow distinct spatial distributions—i.e., $\Sigma_{\text{mix}}(\mathbf{R}) = \sum_{i=1}^{N_{\text{pop}}} \Sigma_i(\mathbf{R})$. The total number of objects has an expectation value $\langle N_{\text{mix}} \rangle = \iint \Sigma_{\text{mix}}(\mathbf{R}) d\mathbf{R} = \sum_{i=1}^{N_{\text{pop}}} \langle N_i \rangle$, where $\langle N_i \rangle = \iint \Sigma_i(\mathbf{R}) d\mathbf{R}$ is the expectation value for the number of objects in the i th subpopulation. The conditional separation function is

$$\mu_{\text{mix}}(s|\mathbf{R}) = \sum_{i=1}^{N_{\text{pop}}} \mu_i(s|\mathbf{R}), \quad (4)$$

where $\mu_i(s|\mathbf{R}) = \int_0^{2\pi} \Sigma_i(\mathbf{R} + \Delta\mathbf{R}) s d\alpha$.

The joint position-separation function is

$$\psi_{\text{mix}}(s, \mathbf{R}) = \sum_{i=1}^{N_{\text{pop}}} \sum_{j=1}^{N_{\text{pop}}} \psi_{i,j}(s, \mathbf{R}), \quad (5)$$

where $\psi_{i,j}(s, \mathbf{R}) \equiv \Sigma_i(\mathbf{R}) \mu_j(s|\mathbf{R})$. The marginal separation function is

$$\phi_{\text{mix}}(s) = \sum_{i=1}^{N_{\text{pop}}} \sum_{j=1}^{N_{\text{pop}}} \phi_{i,j}(s), \quad (6)$$

where $\phi_{i,j}(s) \equiv \iint \psi_{i,j}(s, \mathbf{R}) d\mathbf{R}$. The cross terms are symmetric, such that $\phi_{i,j}(s) = \phi_{j,i}(s)$.

2.2. Binaries

We now consider the separation functions that pertain to a population within which some fraction of the objects are split into binary systems that at position \mathbf{R} , follow internal separation function $\phi_b(s|\mathbf{R})$, normalized so that $\int \phi_b(s|\mathbf{R}) ds = 1$. The surface number density can be written as the sum of contributions from single objects and binary objects: $\Sigma(\mathbf{R}) = \Sigma_s(\mathbf{R}) + \Sigma_b(\mathbf{R})$. We define the binary fraction as $f_b(\mathbf{R}) \equiv \Sigma_b(\mathbf{R})/\Sigma(\mathbf{R})$, such that while $\Sigma(\mathbf{R})$ remains the surface number density of statistically independent objects, the surface number density of countable items is $\Sigma'(\mathbf{R}) = (1 + f_b(\mathbf{R}))\Sigma(\mathbf{R})$ —i.e., a binary system is one object that comprises two countable items. The number of countable items has an expectation value $\langle N' \rangle = \iint \Sigma'(\mathbf{R}) d\mathbf{R} = (1 + f_b) \langle N \rangle$, where $f_b \equiv \langle N \rangle^{-1} \iint f_b(\mathbf{R}) \Sigma(\mathbf{R}) d\mathbf{R}$ is the globally averaged binary fraction.

The joint position-separation function for countable items is (see the derivation in the [Appendix](#))

$$\psi'(s, \mathbf{R}) \approx (1 + f_b(\mathbf{R}))^2 \psi(s, \mathbf{R}) + 2 f_b(\mathbf{R}) \Sigma(\mathbf{R}) \phi_b(s, \mathbf{R}), \quad (7)$$

where $\psi(s, \mathbf{R})$ is the joint position-separation function for independent objects. The approximation is valid as long as the binary separations are small compared to the scale over which $\Sigma(\mathbf{R})$ changes—i.e., $\Sigma(\mathbf{R})$ is approximately constant within the circle shown in Figure 1.

The conditional separation function for countable items is then

$$\begin{aligned} \mu'(s|\mathbf{R}) &= \frac{\psi'(s, \mathbf{R})}{\Sigma'(\mathbf{R})} \\ &\approx (1 + f_b(\mathbf{R})) \mu(s|\mathbf{R}) + \frac{2 f_b(\mathbf{R})}{1 + f_b(\mathbf{R})} \phi_b(s|\mathbf{R}) \end{aligned} \quad (8)$$

,where $\mu(s|\mathbf{R})$ is the conditional separation function for independent objects.

The marginal separation function for countable items is $\phi'(s) = \iint \psi'(s, \mathbf{R}) d\mathbf{R}$. If the binary fraction and internal separation function are both independent of position, such that $f_b(\mathbf{R}) \rightarrow f_b$ and $\phi_b(s|\mathbf{R}) \rightarrow \phi_b(s)$, then the marginal separation function for countable items simplifies to

$$\phi'(s) \approx (1 + f_b)^2 \phi(s) + 2 f_b \langle N \rangle \phi_b(s), \quad (9)$$

where $\phi(s)$ is the marginal separation function for independent objects.

Also, if the binary fraction and internal separation function are independent of position, then the separation functions for countable items integrate to

$$\begin{aligned} \int \mu'(s|\mathbf{R}) ds &\approx (1 + f_b) \langle N \rangle + \frac{2 f_b}{1 + f_b}; \\ \iint \psi'(s, \mathbf{R}) ds d\mathbf{R} &= \int \phi'(s) ds \\ &\approx (1 + f_b)^2 \langle N \rangle^2 + 2 f_b \langle N \rangle. \end{aligned} \quad (10)$$

2.3. Mixtures and Binaries

In the most general case that we consider here, the population consists of a mixture of N_{pop} distinct subpopulations, each independently following its own spatial distribution and each containing binary systems that follow independent internal separation functions. The total surface density is $\Sigma_{\text{mix}}(\mathbf{R}) = \sum_{i=1}^{N_{\text{pop}}} \Sigma_i(\mathbf{R}) = \sum_{i=1}^{N_{\text{pop}}} \Sigma_{s_i}(\mathbf{R}) + \Sigma_{b_i}(\mathbf{R})$, where $\Sigma_{s_i}(\mathbf{R})$ and $\Sigma_{b_i}(\mathbf{R})$ are surface number densities of single and binary objects, respectively, within the i th subpopulation. The total number of statistically independent objects has an expectation value $\langle N_{\text{mix}} \rangle = \iint \Sigma_{\text{mix}}(\mathbf{R}) d\mathbf{R} = \sum_{i=1}^{N_{\text{pop}}} \langle N_i \rangle$, where $\langle N_i \rangle$ is the expectation value for the number of independent objects in the i th subpopulation. The total surface number density of countable items is $\Sigma'_{\text{mix}}(\mathbf{R}) = \sum_{i=1}^{N_{\text{pop}}} \Sigma'_i(\mathbf{R}) = \sum_{i=1}^{N_{\text{pop}}} (1 + f_{b_i}(\mathbf{R})) \Sigma_i(\mathbf{R})$, where $f_{b_i}(\mathbf{R}) = \Sigma_{b_i}(\mathbf{R})/\Sigma_i(\mathbf{R})$ is the local binary fraction of the i th subpopulation. The total number of countable items has an expectation value $\langle N'_{\text{mix}} \rangle = \iint \Sigma'_{\text{mix}}(\mathbf{R}) d\mathbf{R} = \sum_{i=1}^{N_{\text{pop}}} (1 + f_{b_i}(\mathbf{R})) \langle N_i \rangle$.

Generalizing the derivation from [Appendix](#) to include a mixture of subpopulations, the joint position-separation function for countable items is

$$\begin{aligned} \psi'_{\text{mix}}(s, \mathbf{R}) &\approx \sum_{i=1}^{N_{\text{pop}}} \sum_{j=1}^{N_{\text{pop}}} (1 + f_{b_i}(\mathbf{R}) + f_{b_j}(\mathbf{R})) \\ &\quad + f_{b_i}(\mathbf{R}) f_{b_j}(\mathbf{R}) \psi_{i,j}(s, \mathbf{R}) \\ &\quad + 2 \sum_{i=1}^{N_{\text{pop}}} f_{b_i}(\mathbf{R}) \Sigma_i(\mathbf{R}) \phi_{b_i}(s|\mathbf{R}), \end{aligned} \quad (11)$$

where $\phi_{b_i}(s|\mathbf{R})$ is the (normalized) internal separation function for binaries at position \mathbf{R} within the i th subpopulation. The conditional and marginal separation functions for countable items can then be

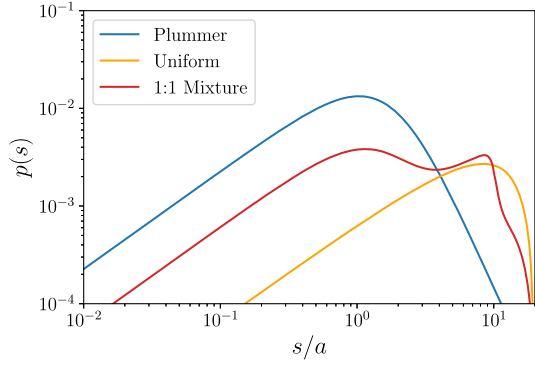


Figure 2. Marginal probability density for pair separations within 1) a Plummer sphere of projected half-light radius a (blue), 2) objects distributed uniformly within a circle of radius $R_{\max} = 10a$ (orange), and 3) a 1:1 mixture of the two (red), for separations up to $2R_{\max}$.

calculated as $\mu'_{\text{mix}}(s|\mathbf{R}) = \psi'_{\text{mix}}(s, \mathbf{R}) / \Sigma'_{\text{mix}}(\mathbf{R})$ and $\phi'_{\text{mix}}(s) = \iint \psi'_{\text{mix}}(s, \mathbf{R}) d\mathbf{R}$, respectively.

If the binary fractions and internal separation functions are all independent of position, then the marginal separation function for countable items is

$$\begin{aligned} \phi'_{\text{mix}}(s) &\approx \sum_{i=1}^{N_{\text{pop}}} \sum_{j=1}^{N_{\text{pop}}} (1 + f_{b_i} + f_{b_j} + f_{b_i} f_{b_j}) \phi_{i,j}(s) \\ &+ 2 \sum_{i=1}^{N_{\text{pop}}} \langle N_i \rangle f_{b_i} \phi_{b_i}(s), \end{aligned} \quad (12)$$

and the joint position-separation function and marginal separation function for countable items integrates to

$$\begin{aligned} \iiint \psi'_{\text{mix}}(s, \mathbf{R}) ds d\mathbf{R} &= \int \phi'_{\text{mix}}(s) ds \\ &\approx \sum_{i=1}^{N_{\text{pop}}} \sum_{j=1}^{N_{\text{pop}}} (1 + f_{b_i} + f_{b_j} + f_{b_i} f_{b_j}) \langle N_i \rangle \langle N_j \rangle \\ &+ 2 \sum_{i=1}^{N_{\text{pop}}} f_{b_i} \langle N_i \rangle. \end{aligned} \quad (13)$$

2.4. Some Useful Cases with Analytic Results

We now consider some specific cases in which the integrals in Equations (1) and (3) can be calculated analytically. First we note that if $\Sigma(\mathbf{R})$ has circular symmetry about the origin, Equations (1) and (3) become

$$\mu(s|\mathbf{R}) = \int_0^{2\pi} \Sigma(\sqrt{R^2 + s^2 + 2Rs \cos \alpha}) s d\alpha \quad (14)$$

and

$$\phi(s) = \int_0^{2\pi} \int_0^\infty \Sigma(R) \mu(s|\mathbf{R}) R dR d\theta, \quad (15)$$

respectively.

2.4.1. Uniform Density in a Circular Field

Consider a population of objects drawn from a (2D) position function that specifies the uniform surface number density $\Sigma_{u,0}$ within a circle of finite radius R_{\max} and zero density at $R > R_{\max}$,

$$\Sigma_u(R) = \Sigma_{u,0} \Theta(R_{\max} - R), \quad (16)$$

where Θ is the Heaviside-Theta function. The number of objects has an expectation value $\langle N_u \rangle = \pi R_{\max}^2 \Sigma_{u,0}$. In terms of dimensionless radius $R_u \equiv R/R_{\max}$ and dimensionless separation variable $s_u \equiv s/R_{\max}$, the conditional separation

function is (via Equation (14))

$$\begin{aligned} \mu_u(s_u|\mathbf{R}) &= \frac{2 \langle N_u \rangle s_u}{\pi R_{\max}} [\pi \Theta(R_{\max}(1 - R_u - s_u)) \\ &+ \left(\pi - \sec^{-1} \left(\frac{-2R_u s_u}{R_u^2 + s_u^2 - 1} \right) \Theta' \right)], \end{aligned} \quad (17)$$

where

$$\Theta' \equiv (-1 + \Theta(R_{\max}[1 - R_u - s_u]))(-1 + \Theta(R_{\max}[s_u - R_u - 1])).$$

The marginal separation function can be derived via multiple methods (Hammersley 1950; Lellouche & Souris 2020) and is given by

$$\phi_u(s_u) = \frac{4 \langle N_u \rangle^2 s_u}{\pi R_{\max}} \left[\cos^{-1} \left(\frac{s_u}{2} \right) - \frac{s_u}{2} \sqrt{1 - \frac{s_u^2}{4}} \right] \quad (18)$$

for $s_u \in [0, 2]$, and $\phi_u(s_u) = 0$ at $s_u > 2$.

2.4.2. Plummer Sphere

The Plummer (1911) model is commonly used to fit the stellar density profiles in dwarf spheroidal galaxies (e.g., McConnachie 2012; Moskovitz & Walker 2020). Objects within a Plummer sphere have positions drawn from

$$\Sigma_p(R) = \frac{\Sigma_{p,0}}{(1 + R^2/a^2)^2}, \quad (19)$$

where the number of stars has an expectation value $\langle N_p \rangle = \pi a^2 \Sigma_{p,0}$ and half the stars are expected to be enclosed within a circle of radius a . Via Equation (14), and in terms of dimensionless separation variable $s_p \equiv s/a$, the conditional separation function is

$$\mu_p(s_p|\mathbf{R}) = \frac{2 \langle N_p \rangle (1 + s_p^2 + R^2/a^2) s_p/a}{[(1 + (R/a - s_p)^2)(1 + (R/a + s_p)^2)]^{3/2}}. \quad (20)$$

Via Equation (15), the marginal separation function is

$$\begin{aligned} \phi_p(s_p) &= \frac{4 \langle N_p \rangle^2 s_p/a}{(4 s_p + s_p^3)^3} [-8 s_p + 2 s_p^3 + s_p^5 \\ &+ 2(1 + s_p^2) \sqrt{4 + s_p^2} \tanh^{-1}(b)], \end{aligned} \quad (21)$$

where $b \equiv \frac{s_p(2 + s_p^2) \sqrt{4 + s_p^2}}{2 + 4s_p^2 + s_p^4}$.

2.4.3. Mixture of Plummer Sphere and Uniform Background

Over the few square degrees (or less) subtended by most dwarf galaxies, stars in the Galactic foreground follow approximately uniform distributions (Irwin & Hatzidimitriou 1995). Therefore most nearby dSphs can be modeled as mixtures of N_{plum} stars that follow a Plummer distribution with Plummer radius a , and N_u stars that follow a uniform distribution over a circular field of radius R_{\max} .

In that case, the conditional separation function, $\mu_{\text{mix}}(s|\mathbf{R})$, is given by Equation (4), with individual terms for uniform and Plummer subpopulations specified by Equations (17) and (20), respectively. The marginal separation function, $\phi_{\text{mix}}(s)$, is given by Equation (6), with analytic contributions from cross terms (see Equation (6)) $\phi_{u,u}(s_u)$, $\phi_{p,p}(s_p)$ and, in terms of

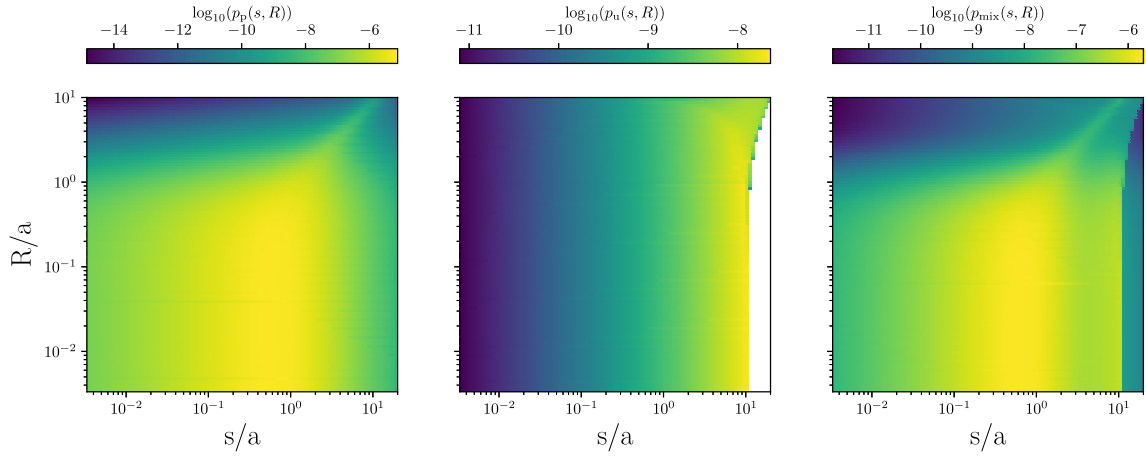


Figure 3. Joint probability density of object positions and pair separations, for (left to right) a Plummer sphere of projected half-light radius a , objects distributed uniformly within a circle of radius $R_{\max} = 10a$, and a 1:1 mixture of the two, for separations up to $2R_{\max}$. In the center panel, whitespace corresponds to regions where $p(s, \mathbf{R}) = 0$ due to the finite field size.

dimensionless separation variable $s_p \equiv s/a$,

$$\phi_{u,p}(s_p) = \phi_{p,u}(s_p) = \frac{N_u N_p s_p (z^2 - s_p^2 + \sqrt{c} - 1)}{z R_{\max} \sqrt{c}}, \quad (22)$$

where $z \equiv R_{\max}/a$ and $c \equiv 1 + z^2 + 2s_p^2(1 - z^2) + s_p^4$.

Figure 2 displays marginal probability densities for separations, $p(s) = \phi(s) / (\int \phi(s) ds)$, for populations of objects that follow a Plummer profile (blue) with scale radius a , and a uniform distribution (orange) within a field of radius $R_{\max} = 10a$. Both curves scale as $p(s) \propto s$ at small separation, reaching maxima at separations near the relevant scale radii of a and R_{\max} , respectively. The red curve indicates the marginal probability density, $p_{\text{mix}}(s) = \phi_{\text{mix}}(s) / (\int \phi_{\text{mix}}(s) ds)$, for a 1:1 mixture of the Plummer and uniform populations, showing local maxima at both characteristic scales.

For the same three cases, the heatmaps in Figure 3 display joint probability densities $p(s, \mathbf{R}) = \psi(s, \mathbf{R}) / (\iiint \psi(s, \mathbf{R}) ds d\mathbf{R})$ and $p_{\text{mix}}(s, \mathbf{R}) = \psi_{\text{mix}}(s, \mathbf{R}) / (\iiint \psi_{\text{mix}}(s, \mathbf{R}) ds d\mathbf{R})$. Separations within the Plummer sphere correlate strongly with position (left panel)—a consequence of the fact that the probability density of radial coordinate R approaches zero as $R \rightarrow \infty$. Thus the rare star at large radius in the Plummer sphere will tend to be widely separated from almost all other stars, which tend to reside at smaller radius. In contrast, the uniform distribution displays no obvious correlation, with the separation density peaking near $s \approx R_{\max}$ except near $R \approx R_{\max}$, where the most probable separation decreases slightly due to the field-edge effect (middle panel).

Figure 4 shows what happens to the marginal probability densities if we add binary components to both uniform and Plummer subpopulations within the 1:1 mixture. In this case, the binary systems within both subpopulations follow a broken power-law separation function (Equation (23)). Parameters of the binary separation function within the uniform subpopulation are held fixed at values chosen to represent observational constraints on wide binaries within the Milky Way halo (Tian et al. 2019), with power-law indices $\gamma_1 = -1.55$, $\gamma_2 = -3.33$, break separation $s_b = 0.001 a$, and smoothing parameter $\Lambda = 0.67$. Panels in Figure 4 then show the effect of varying the binary fraction (left), “outer” power-law index γ_2 (middle), and break separation (right) of the binary separation function within the Plummer subpopulation. In all cases, the marginal

probability density, $p'_{\text{mix}}(s) = \phi'_{\text{mix}}(s) / (\int \phi'_{\text{mix}}(s) ds)$, is now characterized generally by a transition from domination by binaries within the uniform distribution at small separation (where $\phi_{\text{bu}}(s) \propto s^{-1.55}$) to domination by physically unassociated pairs at large separation. Details of the transition change with the binary fraction and separation function that we adopt for the Plummer subpopulation. As the binary fraction within the Plummer subpopulation increases (left panel), the minimum in the $p'_{\text{mix}}(s)$ function shifts toward smaller s , a result of the fact that the separation function for the binaries within the Plummer subpopulation peaks at finite separation $s \sim a$. As the “outer” index γ_2 changes from positive to strongly negative (middle panel), binaries with large separation become scarce within the Plummer subpopulation, and the $p'_{\text{mix}}(s)$ curve increases toward smaller s . Finally, as the break separation increases (right panel), the minimum in the $p'_{\text{mix}}(s)$ function again shifts toward smaller s as a larger fraction of binaries within the Plummer subpopulation have separations $s < s_b$. We emphasize that all of these behaviors can change in detail depending on the binary separation functions assumed for both subpopulations; our purpose here is merely to provide an example of how the observable marginal density $p'_{\text{mix}}(s)$ can be sensitive to the binary separation function that we seek to infer.

3. Application to Dwarf Galaxies

We now apply this formalism to investigate the potential for detectability and characterization of wide binary systems within nearby dwarf galaxies. We generate and analyze mock observational catalogs designed to reproduce the observed structural parameters of the 40 dSph galaxies analyzed by Moskovitz & Walker (2020), with binary companions inserted by hand according to assumed separation functions. The galaxy sample spans a range in luminosity of $10^3 \lesssim L_V/L_{V,\odot} \lesssim 10^7$, Plummer radius $10^1 \lesssim a/\text{pc} \lesssim 10^3$, and distance $20 \lesssim D/\text{kpc} \lesssim 250$, providing a natural “grid” for studying the dependence of detection sensitivity on intrinsic properties.

3.1. Generation of Mock Data

For a given dwarf galaxy, we adopt published values for luminosity, distance, and metallicity from the review of McConnachie (2012), or, when necessary, from more recent discovery papers (e.g., Drlica-Wagner et al. 2015;

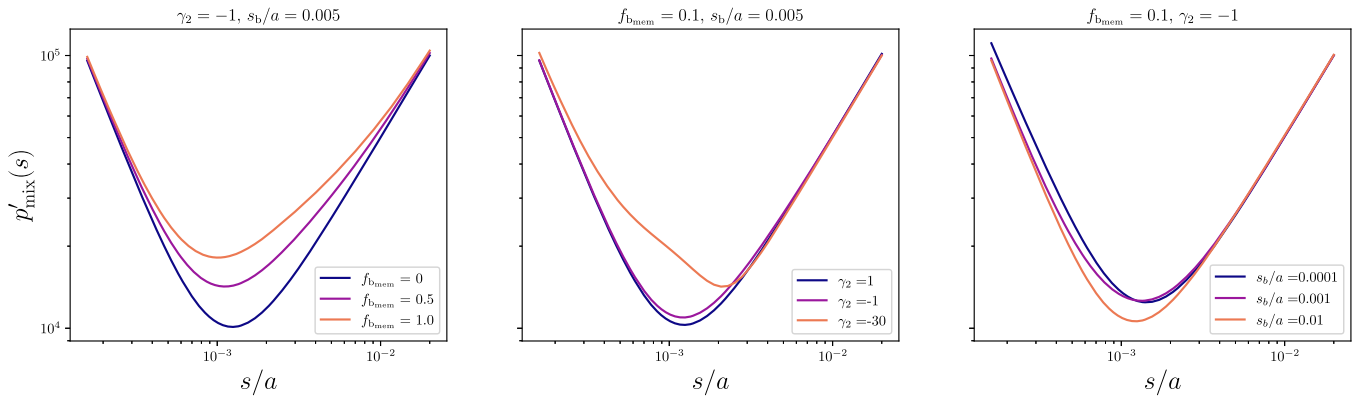


Figure 4. Marginal probability density of pair separations for a 1:1 mixture of Plummer and uniform subpopulations, each containing binary pairs. The separation function for binary pairs within the uniform subpopulation (with a binary fraction of 0.1) follows a fixed broken power law (BpL; Equation (23)), with indices $\gamma_1 = -1.55$ and $\gamma_2 = -3.33$, break separation $s_b = 0.001 a$, and smoothing parameter $\Lambda = 0.67$. Binary pairs within the Plummer subpopulation follow a broken power law with $\gamma_1 = +0.5$, $\Lambda = 0.5$ and the other parameters are allowed to vary. Left, center, and right panels show how the marginal density of pair separations within the mixture varies with binary fraction, power-law index γ_2 , and break separation, respectively, of the binaries within the Plummer subpopulation.

Koposov et al. 2015). We adopt the “circularized” Plummer radii fit by Moskowicz & Walker (2020; fourth column of their Table 3). Given the adopted metallicity and assuming an old (12 Gyr) age, we use PARSEC isochrones and luminosity functions (Bressan et al. 2012; assuming the default Kroupa 2001, 2002 initial mass function) to sample the present-day luminosity function.

We assume that the dSph member subpopulation intrinsically consists of $N_{p_{\text{mem}}}$ “parents” that have positions distributed according to a circular Plummer profile (Equation (19)), and $N_{b_{\text{mem}}}$ “binary companions” to a fraction $f_{b_{\text{mem}}}$ of the parents. We assume that the luminosities of binary companions are drawn independently from the same luminosity function as those of the parent population. We assume that the binary fraction and binary separation function within the dSph member subpopulation are both independent of the parent’s position and luminosity, with the separation function, $\phi_{\text{mem}}(s)$, following one of three distinct functional forms, discussed in detail in Section 3.2.

We assume that the dwarf galaxy is observed against a foreground subpopulation of Milky Way stars that consists of parents following a uniform spatial distribution within a circular field of radius $R_{\text{max}} = 10$ times the Plummer radius of the dwarf galaxy, and binary companions to a fraction $f_{b_{\text{non}}}$ of these parents. We assume that within this field, the number of detected (i.e., brighter than the adopted magnitude limit) parents within the nonmember subpopulation equals the number of detected parents within the dSph member subpopulation. We assume that the binary fraction and binary separation function within the nonmember subpopulation are both independent of position, with the separation function, $\phi_{\text{non}}(s)$, following an observationally motivated BPL (Section 3.2).

We construct a mock observational catalog as follows:

1. Draw N_{mem} luminosities randomly from the present-day stellar luminosity function. The value of N_{mem} , the number of stars belonging to the dwarf galaxy (including parents and binary companions), is set by the requirement that the cumulative luminosity equal the published galaxy luminosity.
2. Given the adopted member binary fraction, randomly assign each member star the status of either “parent” or “binary companion”.

3. For each parent in the member subpopulation, assign a 2D position by sampling the radial coordinate R from a Plummer distribution having the published Plummer radius, and position angle θ from a uniform distribution between $0 \leq \theta \leq 2\pi$.
4. For each binary companion in the member subpopulation, assign a 2D position by offsetting from a randomly chosen (without replacement) parent by a 2D vector $\Delta\mathbf{R}$. Draw the magnitude $|\Delta\mathbf{R}| = s$ from the adopted member binary separation function (Section 3.2), and the direction angle from a uniform distribution between $0 \leq \alpha \leq 2\pi$.
5. Impose observational resolution and magnitude limits by 1) combining into a single point source any pairs separated by less than an assumed resolution limit r_{lim} , and 2) discarding any source fainter than an assumed limiting magnitude m_{lim} .
6. Add foreground nonmembers by repeating step 3, but for $N_{p_{\text{non}}}$ nonmember parents (all of which are assumed to be brighter than the adopted magnitude limit) with 2D positions drawn from a uniform spatial distribution over a circle of radius $R_{\text{max}} = 10$ times the dSph Plummer radius. Then, to a fraction $f_{b_{\text{non}}}$ of the nonmember parents (drawn randomly without replacement), add a binary companion with position offset as described in step 4, drawing the magnitude of the offset from $\phi_{\text{non}}(s)$. Since the separation function is expressed in physical units (Section 3.2), convert into angular offsets (assuming the sky is flat over the observed field) by assuming a characteristic nonmember distance of 10 kpc.
7. In order to mimic observational errors in the measurement of centroids, scatter the position of each point source by a 2D vector drawn randomly from a bivariate Gaussian that is centered on the true location and has a covariance matrix given by $0.5 r_{\text{lim}} I_2$, where I_2 is the 2×2 identity matrix.

We adopt fiducial values of $V_{\text{lim}} = 27$ and $r_{\text{lim}} = 0''.05$ for the magnitude and resolution limits, respectively. For the member subpopulation, we adopt a binary fraction such that a fraction $f_{b_{\text{mem}}} = 0.1$ of member parents have a binary companion with separation $s < 5$ pc that is drawn from the initial broken power-law model (without the imposed upper limit, the total number of separations diverges when $\gamma_2 \geq -1$). This fraction then effectively decreases for the truncated

power-law input and increases for Öpik’s law input, as discussed in Section 3.2.

The empirically motivated separation function that we adopt for nonmembers is a BPL that diverges toward $s \rightarrow 0$ (Section 3.2). Therefore we choose the nonmember binary fraction such that the number of nonmember binary companions that are separated from their parents by more than the adopted resolution limit equals 0.1 times the number of nonmember parents.

After imposing these limits, the number of “detectable” binary systems within both member and nonmember sub-population—i.e., pairs separated by more than the adopted resolution limit and for which both members are brighter than the adopted magnitude limit—ranges from a few to $\sim 10^4$.

We reiterate that the wide binary fraction within dwarf galaxies is currently unconstrained observationally. While Longhitano & Binggeli (2010) infer a wide binary fraction of $\sim 10\%$ within the solar neighborhood, this constraint is not necessarily relevant for the older, more metal-poor stellar populations that occupy the denser dark matter halos of dwarf galaxies. Our assumption that $f_{\text{bmem}} = 0.1$ for the broken power-law separation function is meant only to provide—given the range of luminosities and distances among the known dwarf galaxies—a corresponding range in detectability of their wide binary populations. While the mock wide binary populations provide some basis for comparing relative detectability across different dwarf galaxies, and for testing performance as a function of number of detectable wide binaries, they should not be interpreted as forecasts of wide binary populations—either in individual dSphs or in the dSph population.

3.2. Input Binary Separation Functions

Separations between companions within binary star systems are set by the physics of star formation/evolution and interactions with the ambient medium (Chandrasekhar 1944; Heggie 1975; Bahcall et al. 1985; Weinberg et al. 1987; Jiang & Tremaine 2010; Kouwenhoven et al. 2010; Peñarrubia 2021). As such, binary separations can be independent of the density field, $\Sigma(\mathbf{R})$, of the parent stellar population—at least on scales smaller than the characteristic parent separation—and the binary separation function can be modeled directly using simple analytic formulae.

For example, Öpik (1924) proposes a log-uniform binary separation function, $\phi(s) \propto s^{-1}$, which is typically observed within young star clusters and stellar associations (Kouwenhoven et al. 2007; Kraus & Hillenbrand 2008). Working primarily with short-period binary systems within the solar neighborhood, Duquennoy & Mayor (1991) and Raghavan et al. (2010) fit log-normal period distributions that, assuming uniform distributions of eccentricity and mass ratio, correspond approximately to log-normal separation functions. In order to allow for a characteristic scale for wide binary formation/destruction, others have adopted a BPL (e.g., Andrews et al. 2017; El-Badry & Rix 2018; Tian et al. 2019),

$$\phi(s) = \phi_0 \left(\frac{s}{s_b} \right)^{\gamma_1} \left[\left(1 + \left(\frac{s}{s_b} \right)^{\frac{1}{\Lambda}} \right) \right]^{(\gamma_2 - \gamma_1)\Lambda}, \quad (23)$$

such that near a “break” separation s_b , the power-law index changes from “inner” value γ_1 to “outer” value γ_2 , at a rate controlled by the smoothing parameter Λ .

For the purpose of testing our methodology, we generate mock data sets for which the wide binary populations follow theoretically and/or observationally motivated separation functions.

We glean theoretical motivation from the work of Peñarrubia (2021, “P21” hereafter), who conducts N -body experiments to study the formation of wide binaries via dynamical capture within the tidal debris of disrupting star clusters. While this formation process is stochastic, the resulting pairs follow a universal semimajor axis distribution that scales as $p(a) \propto a^{1/2}$, with a normalization that scales with progenitor cluster mass as $N_b \propto M^{1/2}$. Subsequently, perturbative encounters with “clumpy” substructures (e.g., dark matter subhalos) cause the separation function to evolve toward Öpik’s law beyond a characteristic separation that decreases with time. Simultaneously, beyond another characteristic separation that depends on the smooth component of the host’s gravitational potential, tidal forces steepen the separation function more dramatically, over time approaching a sharp truncation. We note that other mechanisms can also affect the wide binary separation function; for example, Hernandez & Lee (2008) show that wide binaries embedded within a smooth dark matter fluid will harden due to dynamical friction. While it may in practice be difficult to disentangle the above mechanisms, it is noteworthy that all work against survival of the widest binary systems.

Equation (23), but with parameters chosen to represent different combinations of the processes simulated by P21.

1. *Broken power law:* The first input separation function follows a BPL with index changing smoothly ($\Lambda = 0.5$) from $\gamma_1 = +0.5$ to $\gamma_2 = 1$ around break separation $s_b = 0.5$ pc. Following P21, this behavior represents a wide binary population that forms via dynamical capture and evolves only mildly due to encounters with perturbers (see the right panel of P21’s Figure 8).

As stated in Section 3.1, for the BPL model we adopt a member binary fraction of $f_{\text{bmem}} = 0.1$; the fraction of member parents that have detectable binary companions (i.e., separated by more than the adopted resolution limit) is smaller by an amount that depends on the distance to the dSph.

2. *Truncation:* The second input separation function follows a BPL with index changing sharply ($\Lambda = 0.01$) from $\gamma_1 = +0.5$ to $\gamma_2 = -\infty$ around $s_b = 0.5$ pc. This behavior represents the truncation that results from tidal disruption of wide binaries in the smooth potential of the host system (see the left panel of P21’s Figure 8).

In practice, we generate realizations of the truncation model simply by removing from the BPL case any binary companions that are separated from their parents by $s > 0.5$ pc.

3. *Öpik’s law:* The third input separation function is Öpik’s law, which we recover by setting $\gamma_1 = \gamma_2 = -1$. Physically, this case can represent a scenario in which the wide binary population has evolved strongly due to encounters with perturbers, such that the break separation has shrunk to a scale much smaller than the instrumental resolution limit.

We generate realizations of Öpik’s law by drawing separations from a probability distribution $\phi_{\text{mem}}(s) \propto s^{-1}$, subject to the constraint that the number of separations at $s > 0.5$ pc be unchanged with respect to the original BPL sample.

Table 1
Free Parameters and Adopted Priors

Free Parameter	Description	Range of Uniform Prior	Equation Reference
$\log_{10}(a)$	Plummer scale radius (radians)	$(-6, -1)$	19
$\log_{10}\langle N'_{\text{mem}} \rangle$	Expectation value for the number of member stars	$(-2, 6)$	19
$\log_{10}\langle N'_{\text{non}} \rangle$	Expectation value for the number of nonmember stars	$(-2, 6)$	16
<i>Binary Separation Function: Members</i>			
$\log_{10}(f_{\text{bmem}})$	Binary fraction ($f_{\text{bmem}} = N_{\text{bmem}}/N_{\text{pmem}}$)	$(-5, 0)$	23
γ_1	Inner power-law index	$(-2, 1)$	23
$\gamma'_2 = \frac{-\gamma_2}{\gamma_2 - 2}$	Outer power-law index	$(-1, 1)$	23
s_{bmem}	Break separation (radians)	$(0, 2 \text{ pc}/D)$	23
$\log_{10}(\Lambda)$	Smoothing parameter	$(-2, 0)$	23
<i>Binary Separation Function: Nonmembers</i>			
$\log_{10}(f_{\text{bnon}})$	Binary fraction ($f_{\text{bnon}} = N_{\text{bnon}}/N_{\text{pnon}}$)	$(-5, 0)$	23
γ_1	Inner power-law index	$(-5, -1)$	23
γ_2	Outer power-law index	$(-5, -1)$	23
s_{bnon}	Break separation (radians)	$(0, 2 \times 10^{-4})$	23

Finally, to the subpopulation that represents contaminating Milky Way foreground, we assign binary separations motivated by observational constraints. Specifically, we assume that at wide separations, foreground binaries follow the BPL that characterizes “halo-like” binaries in the analysis of Gaia data by Tian et al. (2019): $(\gamma_1, \gamma_2, \log(s_b/\text{AU}), \Lambda) = (-1.55, -3.33, 4.59, 0.67)$.

3.3. Fitting Method

For each mock dSph, we use Bayesian inference to estimate the posterior probability density in the space defined by parameter vector θ , where θ specifies the surface density profiles and binary separation functions of “member” (i.e., dSph) and “nonmember” (Galactic foreground) subpopulations. Given the data vector \mathbf{D} , the posterior probability is

$$p(\theta|\mathbf{D}) = \frac{p(\mathbf{D}|\theta)p(\theta)}{p(\mathbf{D})}, \quad (24)$$

where $p(\mathbf{D}|\theta)$ is the likelihood of the data given the model specified by θ , $p(\theta)$ is the prior probability distribution, and $p(\mathbf{D}) = \int_{\theta} p(\mathbf{D}|\theta)p(\theta)d\theta$ is the marginal likelihood.

Supposing the observational data consists of cataloged positions for N detected stars, we consider the data vector \mathbf{D} that comprises all off-diagonal elements of the $N \times N$ matrix whose i, j element is given by $(\mathbf{R}_i, s_{i,j})$, where $s_{i,j} \equiv |\mathbf{R}_i - \mathbf{R}_j|$. Neglecting observational errors and covariance among the nonindependent discrete data points in \mathbf{D} , we approximate the likelihood function as⁵

$$p(\mathbf{D}|\theta) \approx \prod_{i \neq j}^N \frac{\psi'_{\text{mix}}(s_{i,j}, \mathbf{R}_i|\theta)\psi'_{\text{mix}}(s_{j,i}, \mathbf{R}_j|\theta)}{\left(\iint_{\text{field}} \int_{s_{\text{min}}}^{s_{\text{max}}} \psi'_{\text{mix}}(s, \mathbf{R}|\theta) ds d^2\mathbf{R} \right)^2}, \quad (25)$$

where $\psi'_{\text{mix}}(s, \mathbf{R}|\theta)$ is given by Equation (11). Limits in the normalizing integral can be adjusted to account for observational selection imposed, e.g., by resolution limits and finite survey area. Here we set s_{min} equal to the assumed angular

resolution limit of $0''.05$, and set s_{max} equal to the angle corresponding to a physical separation of 2 pc at the distance to the dSph (pairs with larger separations are not included when evaluating Equation (25)). Imposing such a finite upper limit is not strictly necessary, but can make more efficient use of computational resources, as large separations contain little information about the binary population.

When fitting the data set, we assume the dSph member subpopulation follows a Plummer profile with a binary separation function given by the BPL of Equation (23); in order to allow the outer index γ_2 to reach very negative values (mimicking truncation) without unduly skewing its prior, we fit instead a rescaled parameter, $\gamma'_2 \equiv -\gamma_2/(\gamma_2 - 2)$, with a uniform prior between $-1 \leq \gamma'_2 \leq +1$. For the nonmember subpopulation, we assume a uniform 2D spatial distribution and a binary separation function that also follows the BPL form of Equation (23), with smoothing parameter fixed at $\Lambda = 0.5$. Table 1 lists the 12 free model parameters and identifies boundaries of the uniform priors that we adopt.

We note that all of the three binary separation functions used to generate the mock data (Section 3.1) are special cases of the BPL that we adopt when modeling the data. Of course there is no guarantee that this model will be adequate when applied to real data. In practice, it may be necessary to experiment with alternative models (e.g., a log-normal separation function, which has been used to describe the distribution of short-period binary separations in the solar neighborhood; Raghavan et al. 2010) and apply standard criteria (e.g., information criteria or the Bayesian evidence ratio) for model selection. In order to investigate the effect of model selection on the inferred binary population, we repeated our analysis for an additional suite of mock data sets wherein the input binary separation function followed a log-normal distribution (with mean $\log_{10}[s/\text{pc}] = -0.8$ and standard deviation $\sigma_{\log_{10}[s/\text{pc}]} = 0.4$), with an identical number of detectable binary pairs as in the smooth BPL case. We then continued to adopt the BPL model when fitting the data. For each of the mock galaxies having more than 2000 detectable binary pairs (i.e., those in Figure 5), we confirm that even when adopting the wrong input model, we reliably recover the input number of detectable binary pairs. This experiment provides reassurance that at least for samples of the

⁵ We expect stellar centroid errors to be smaller than s_{min} for stars detected at sufficient signal-to-noise ratio to be included in observational catalogs. Covariance, however, is necessarily present among the discrete data points in \mathbf{D} as separations between pairs of objects are not independent; our test results include any errors introduced by neglecting this effect.

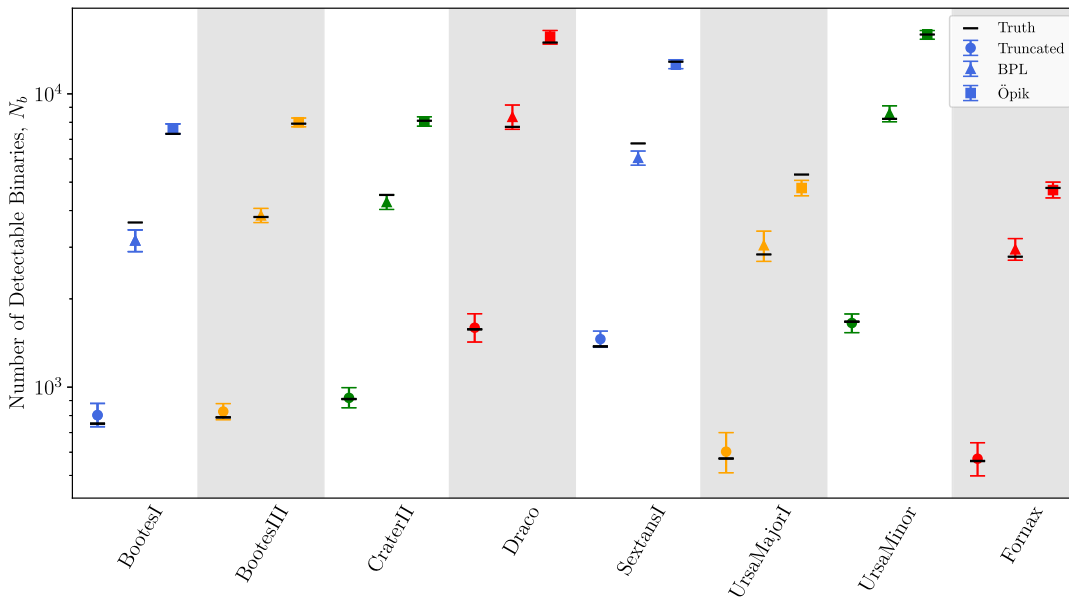


Figure 5. Number of detectable (i.e., separation smaller than the adopted resolution limit, both sources brighter than the adopted magnitude limit) binary systems within the dSph member subpopulation, as inferred by applying our analysis to mock data wherein the dSph binary population follows 1) a BPL, 2) a truncated power law, and 3) Öpik’s law, for mock dSphs containing more than 2000 detectable binaries. Data points and error bars represent median and 95% credibility intervals from posterior probability distribution functions; black tick marks identify true input values. Marker color is intended only to aid the eye in grouping results together for a given dSph.

size and quality considered here, model mismatch is not a source of significant systematic error.

We use the software package MultiNest (Feroz & Hobson 2008; Feroz et al. 2009), and in particular, its Python wrapper, PyMultiNest (Buchner et al. 2014), to estimate model parameters. MultiNest uses a nested sampling algorithm (Skilling 2004) to compute the marginal likelihood, a procedure that also provides random samples drawn from the posterior probability distribution function.

In practice, we adopt a two-step procedure in which we estimate stellar surface density profile parameters (first three rows of Table 1) separately from the binary separation functions. In the first step, we fit only the stellar density profile. Assuming the number of stars observed within an area element is a Poisson random variable, the data set of stellar positions, $D_{\mathbf{R}}$, has the log-likelihood (Richardson et al. 2011)

$$\ln p(D_{\mathbf{R}}|\theta) = \sum_{i=1}^N \ln(\Sigma'_{\text{mix}}(\mathbf{R}_i|\theta)) - \iint_{\text{field}} \Sigma'_{\text{mix}}(\mathbf{R}|\theta) d^2\mathbf{R}, \quad (26)$$

where $\Sigma'_{\text{mix}}(\mathbf{R}|\theta) = \Sigma'_{\text{mem}}(\mathbf{R}) + \Sigma'_{\text{non}}(\mathbf{R})$ is the surface number density of countable stars at position \mathbf{R} , given the model specified by θ . Using the likelihood given by Equation (26), we run MultiNest to obtain a random sample from the posterior probability distribution for the expectation value for the number of member stars, $\langle N'_{\text{mem}} \rangle$, the expectation value for the number of nonmember stars, $\langle N'_{\text{non}} \rangle$, and the Plummer radius, a , of the member subpopulation.

In the second step, we run MultiNest using the full likelihood function given by Equation (25), obtaining random samples from posteriors for parameters that specify binary separation functions (rows 4–12 of Table 1) for member and nonmember subpopulations. In this second step, for each likelihood evaluation, we draw values of $\langle N'_{\text{mem}} \rangle$, $\langle N'_{\text{non}} \rangle$ and a randomly from the posterior obtained in step 1.

4. Results

Here we present results from our analysis of the mock data sets described in Section 3. In general, the initial fits to surface density profiles accurately recover input parameters; we do not display these results here, as our procedure for fitting surface density is already standard practice. Instead, we focus on our inference of binary separation functions for dSph member subpopulations. Figures 5–10 summarize the posterior probability distribution functions that we estimate for parameters that specify the separation function $\phi_{\text{bmem}}(s)$. For each of the three input separation functions for each dSph, we plot the median of the posterior probability distribution function inferred for each parameter, with error bars enclosing the 95% credible region. Black tick marks indicate true input values.

Figures 5 and 6 show our inferences for the number of detectable binary systems (i.e., pairs whose members are separated by more than the adopted resolution limit and are individually brighter than the adopted magnitude limit) within the member subpopulation, for dSphs where the input number is larger than 2000 and smaller than 200, respectively. While not explicitly a free parameter, the number of detectable binaries is a straightforward combination of the inferred number of member stars (brighter than the adopted magnitude limit), the inferred member binary fraction, and the integral of the inferred member binary separation function over separations larger than the adopted resolution limit.

For the samples having more than 2000 detectable binary systems, Figures 7 and 8 display inferences for the “inner” and “outer” power-law indices, γ_1 and $\gamma_2' \equiv -\gamma_2/(\gamma_2 - 2)$, respectively. Figure 9 displays results for the break separation, s_b , and Figure 10 shows results for the smoothing parameter, Λ .

We find that our posteriors generally track the input values. For the number of detectable binary systems, this success holds even as the number of detectable binaries approaches zero (Figure 6), providing some reassurance that we are not prone to

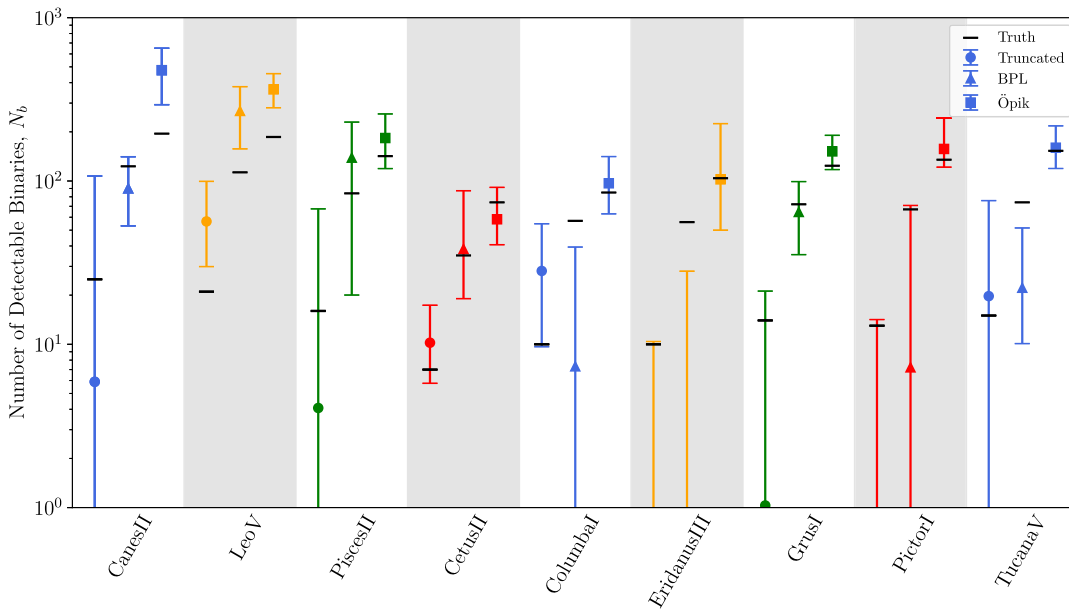


Figure 6. Same as Figure 5 for mock dSphs containing fewer than 200 detectable binary systems.

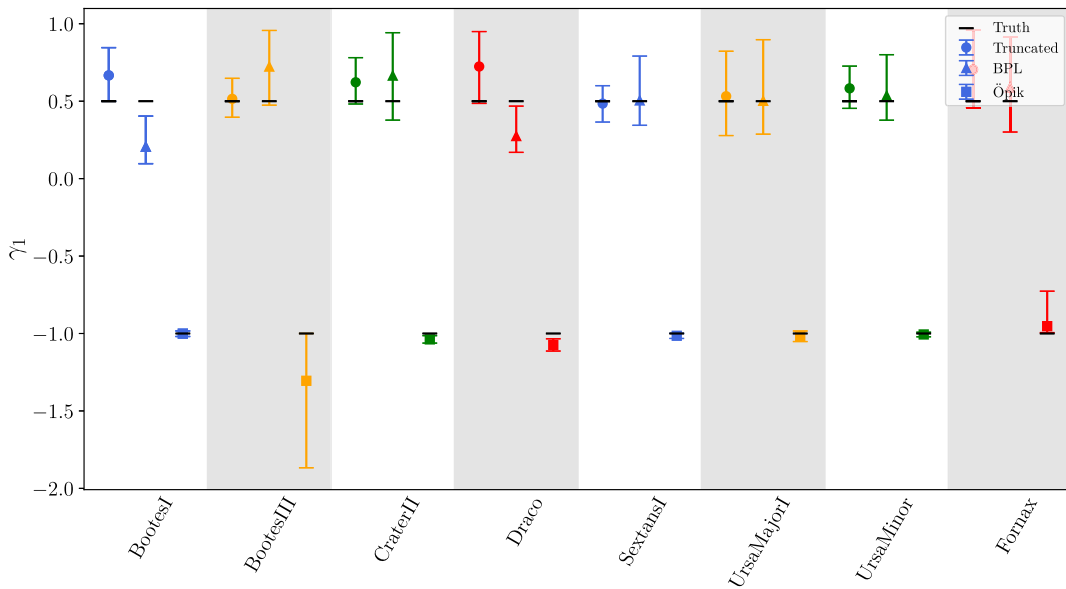


Figure 7. Inference of the inner power-law index, γ_1 , of the binary separation function that governs the dSph member subpopulation for dSphs with more than 2000 detectable binary systems. Data points and error bars represent median and 95% credibility intervals from posterior probability distribution functions; black tick marks identify true input values.

making spurious detections of binary systems. Of course, lack of detectable binaries precludes meaningful inference of the binary separation function; indeed, as the number of detectable binaries decreases toward zero, our posteriors for separation function parameters become dominated by the priors listed in Table 1.

Figures 11 and 12 show how our fitted models compare directly to the mock separation data generated for Ursa Minor and Cetus II, chosen to represent cases that are rich and poor, respectively, in detectable binary systems. Left, center, and right panels show marginal densities of pair separations, with input separation functions for member stars following the BPL (left), truncated power law (center), and Öpik’s law (right).

Overplotted are the input model (red curve), as well as 95% intervals depicting the prior (dotted black curves) and posterior (orange interval) probability distributions. The top panels show the total separation function observed for all pairs, $p'_{\text{mix}}(s)$, regardless of whether the objects are physically associated. The bottom panels depict only the separations between physically associated binaries within the member subpopulation, $\phi_{\text{mem}}(s)$.

We see that for the mock Ursa Minor, which contains $\gtrsim 3000$ detectable binaries, the posterior intervals for $p'_{\text{mix}}(s)$ are difficult to distinguish by eye from the input models. For the mock Cetus II, which contains $\sim 10\text{--}100$ detectable binaries depending on the input model, the posterior intervals for $p'_{\text{mix}}(s)$ are obviously wider than for UMi, but still agree well

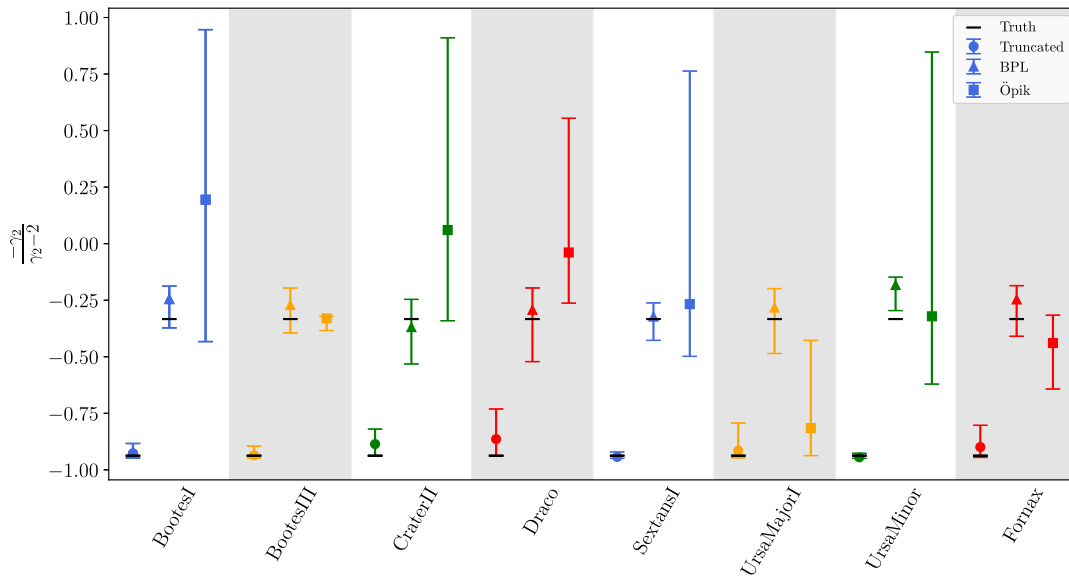


Figure 8. Inference of the outer power-law index parameter, $\gamma_2' \equiv -\gamma_2/(\gamma_2-2)$, of the binary separation function that governs the dSph member subpopulation for dSphs with more than 2000 detectable binary systems. Data points and error bars represent median and 95% credibility intervals from posterior probability distribution functions; black tick marks identify true input values (omitted for Öpik’s law inputs).

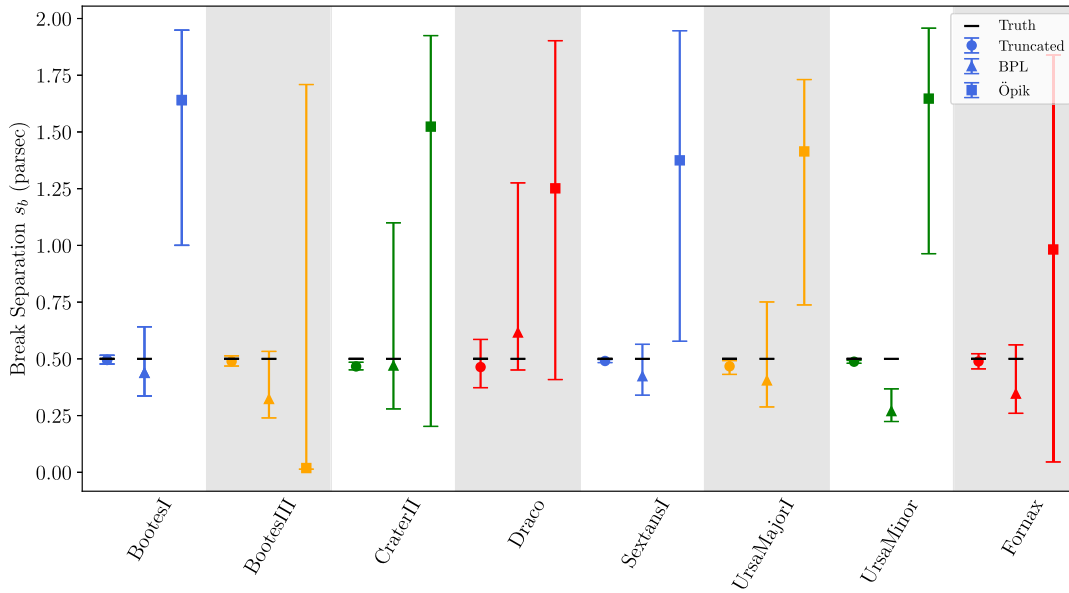


Figure 9. Inference of the break separation, s_b , of the binary separation function that governs the dSph member subpopulation for dSphs with more than 2000 detectable binary systems. Data points and error bars represent median and 95% credibility intervals from posterior probability distribution functions; black tick marks identify true input values (omitted for Öpik’s law inputs).

with the input models. This is indicative that even data sets containing $\mathcal{O}(10)$ detectable binaries can be informative about the separation function.

We now discuss behaviors that are specific to each of the three input models for the member binary separation function.

4.1. Broken Power Law

When the input binary separation function follows the (untruncated) BPL, we find that the posteriors for both the inner and outer power law indices are generally consistent with input values of $\gamma_1 = +0.5$ and $\gamma_2 = -1$ (triangular markers in Figures 5–10). Moreover, when the number of detectable binaries exceeds a few hundred, there is sufficient precision to

detect the transition around the break separation, as can be seen in the simultaneous constraints on γ_1 , γ_2 and s_b . However, in modeling the transition, there is some degeneracy among the outer power-law index, the break separation, and the smoothing parameter. This degeneracy can be seen in Figure 13, which displays as a representative example the multidimensional posterior that we obtain for the mock data set for Ursa Minor in the case of input separation function given by the BPL.

4.2. Truncated Power Law

When the input model follows the truncated power law, we see that our posteriors can accurately recover the abrupt transition from $\gamma_1 = +0.5$ to $\gamma_2 = -\infty$ (circular markers in

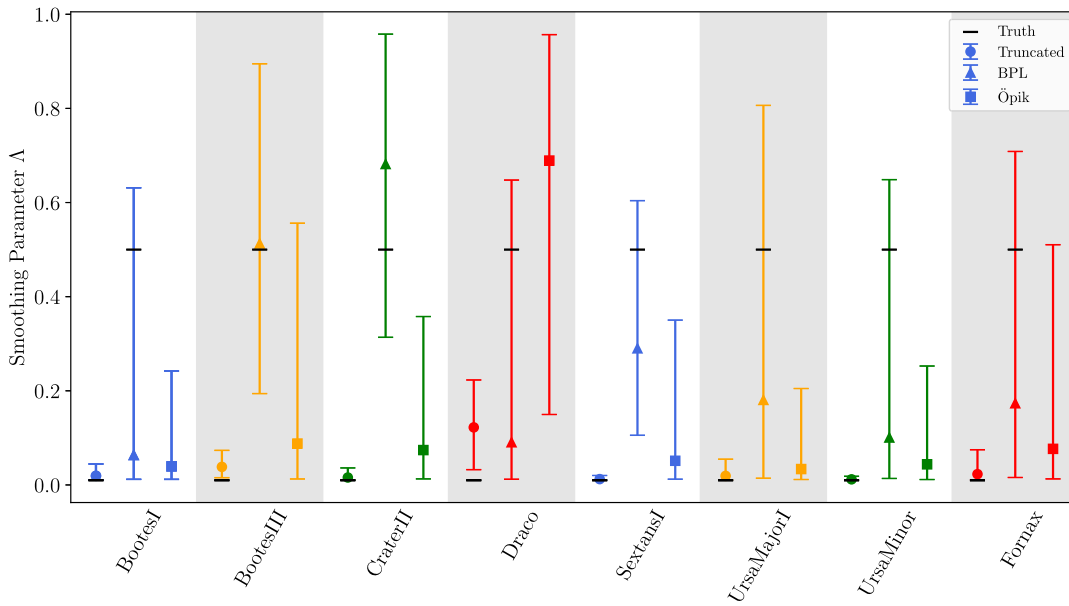


Figure 10. Inference of the smoothing parameter, Λ , of the binary separation function that governs the dSph member subpopulation for dSphs with more than 2000 detectable binary systems. Data points and error bars represent median and 95% credibility intervals from posterior probability distribution functions; black tick marks identify true input values.

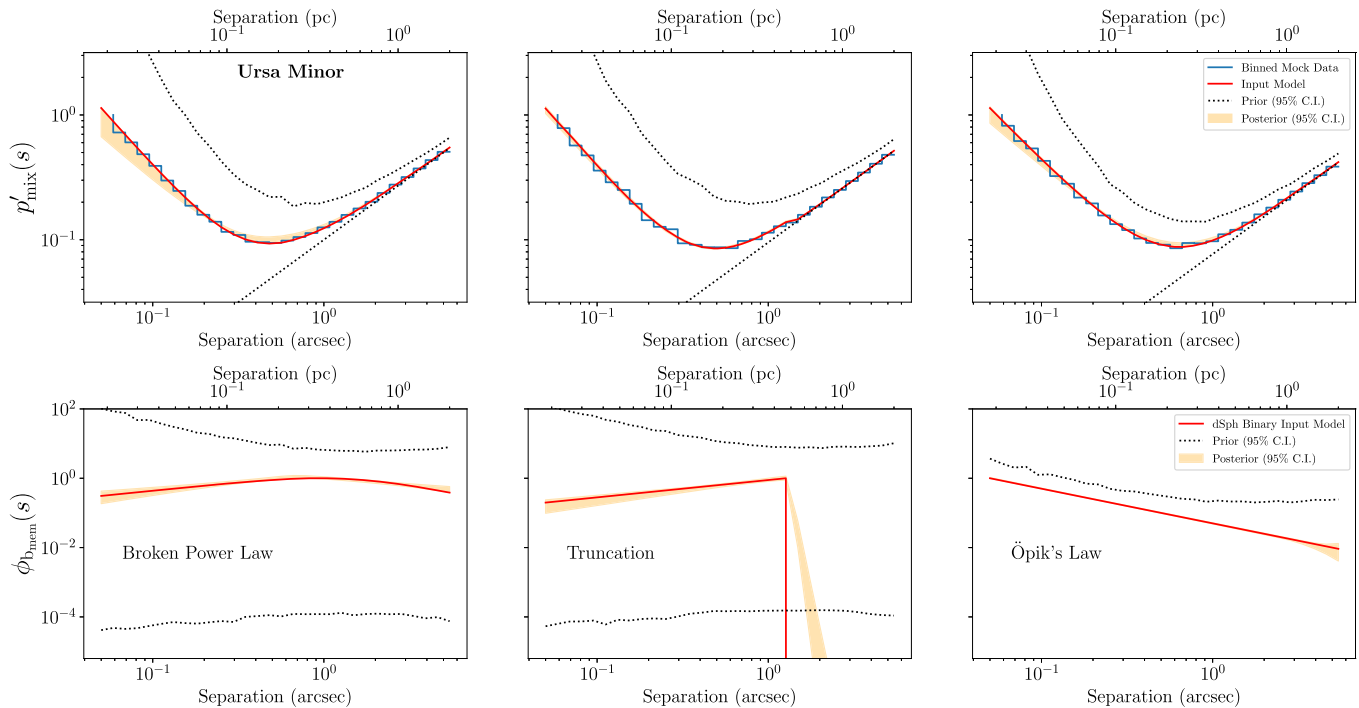


Figure 11. Marginal density of pair separations from mock data sets drawn for Ursa Minor, with input binary separation function for dSph member stars following a truncated power law (left), BPL (center), and Öpik's law (right). In the top row, histograms depict all pair separations regardless of physical association. Overplotted are the input model (red) and 95% credibility intervals from the prior probability distribution (enclosed by dashed black lines) and the posterior probability distribution (orange band) that we obtain by fitting the joint distribution of pair separations and object positions. The distributions in the bottom panels pertain only to separations between physically associated pairs within the dSph member subpopulation.

Figures 5–10). Here we find that the inner power-law index tends to be tightly constrained around the input value of $\gamma_1 = +0.5$. Sensitivity to a sharp truncation is reflected in the posteriors for the outer power-law index, the smoothing parameter, and the break separation. The posterior for γ_2'

pushes up against the edge of the prior at $\gamma_2' = -1$, corresponding to $\gamma_2 = -\infty$ (because the input value is at the edge of the prior, no finite posterior interval will include the input value). Likewise, the posterior for the smoothing parameter pushes against the lower edge of its prior, indicating

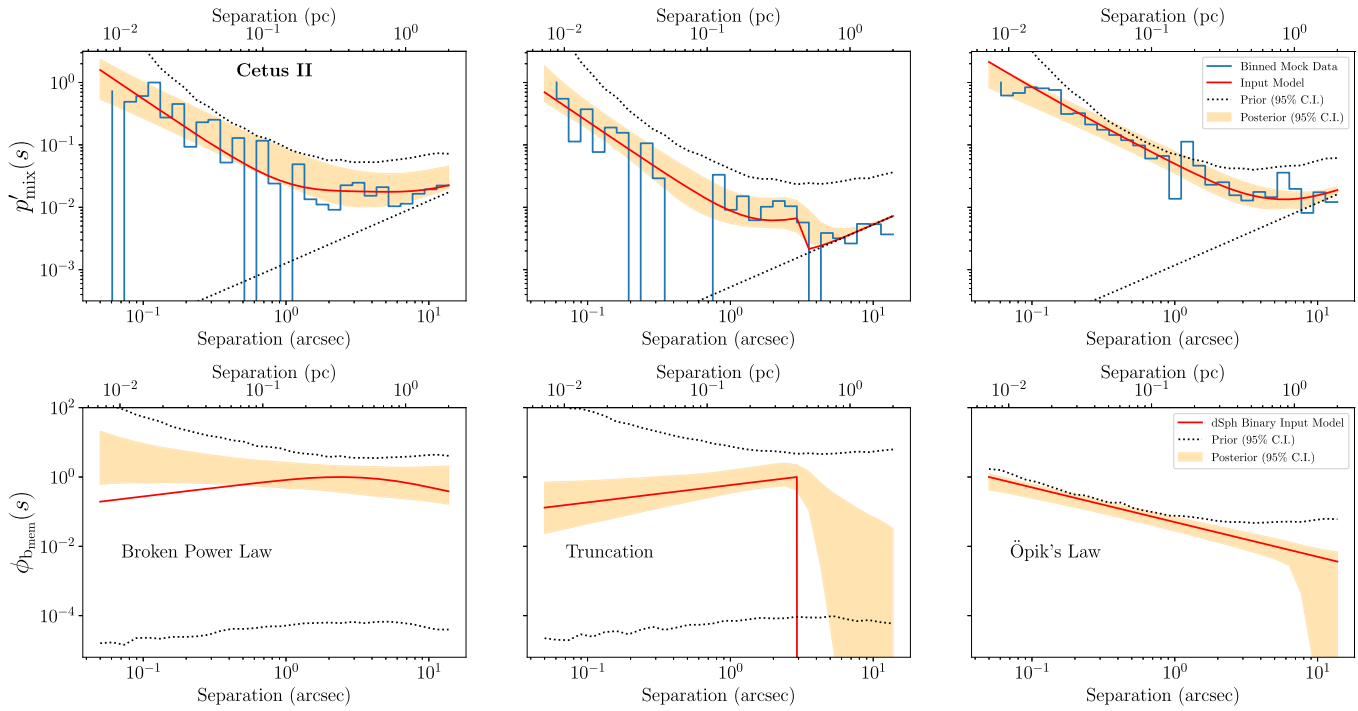


Figure 12. Same as Figure 11, but for mock data sets for Cetus II.

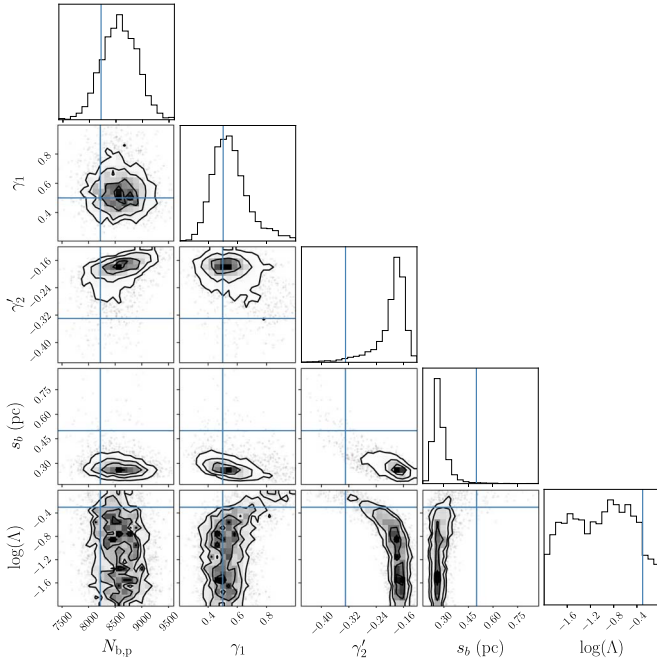


Figure 13. Example of multidimensional posterior probability distributions inferred for parameters that specify the binary separation function for the dSph member subpopulation, from the mock UMi data set with BPL input model. Contours represent 68%, 95%, and 99% credible intervals, and blue crosshairs mark input values.

a sharp transition. As a result, the break separation is tightly constrained around its input value. Again, to provide a representative example, Figure 14 shows the multidimensional posterior obtained for the mock Ursa Minor, with the input separation function given by the truncated power law.

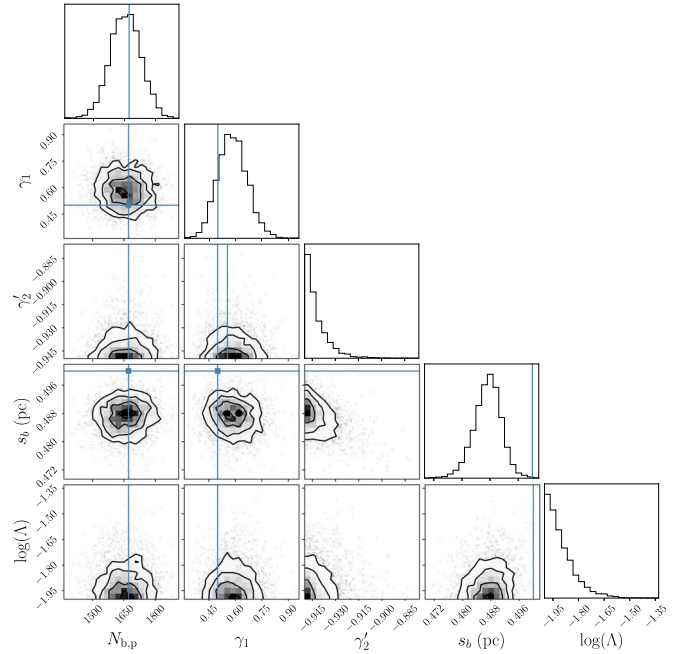


Figure 14. Same as Figure 13, but for the truncated power law as the input model.

4.3. Öpik's Law

Finally, when the input model follows Öpik's law, our posteriors accurately recover the unbroken power-law index of $\gamma_1 = -1$, albeit via a combination of the now-redundant index parameters γ_1 and γ_2 (square markers in Figures 5–10). Figure 15 again shows the multidimensional posterior obtained for Ursa Minor, only with the input separation function

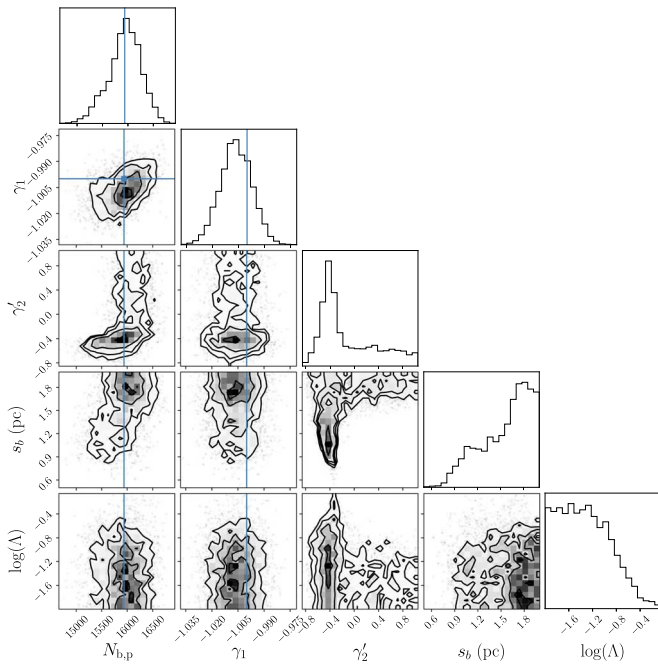


Figure 15. Same as Figure 13, but for Öpik’s law as the input model.

following Öpik’s law. The index parameters γ_1 and γ_2' both have prominent peaks at values consistent with Öpik’s law ($\gamma_1 = -1$, $\gamma_2' = -1/3$); however, depending on whether the break separation parameter is smaller than s_{\min} , larger than the maximum separation s_{\max} , or somewhere in between, the separation function between s_{\min} and s_{\max} is controlled by γ_2 , γ_1 , or a combination wherein both have values corresponding to Öpik’s law, respectively. This behavior is reflected in the fact that γ_2 is tightly constrained around a value of -1 when the break separation is small, but is virtually unconstrained when the break separation is large.

5. Summary and Discussion

We have introduced and developed new analytical tools for the detection and characterization of wide binary systems from catalogs of 2D object positions. Specifically, we have derived general formulae for calculating the conditional separation function $\mu(s|\mathbf{R})$, the joint position-separation function $\psi(s, \mathbf{R})$, and the marginal separation function $\phi(s)$ for any population of objects with specified position function $\Sigma(\mathbf{R})$. Moreover, the object population can be a mixture of an arbitrary number of subpopulations, each of which can have some position-dependent fraction of its objects split into binary systems that follow arbitrary and position-dependent internal separation functions $\phi_b(s|\mathbf{R})$. We have derived analytic separation functions under conditions that surface density follows a circularly symmetric Plummer profile and/or a uniform distribution within a finite circular field. We have used these results to analyze mock stellar position data sets that we generated to mimic the observed structural parameters of the Milky Way’s known dSph satellites, inserting wide binary populations by hand according to different separation functions that represent different scenarios for wide binary evolution. We have demonstrated the ability to recover input parameters that govern binary separation functions, even when the observed sample contains as few as $\mathcal{O}(10)$ binary objects in the member subpopulation.

All of this bodes well for the study of wide binaries within dwarf galaxies, which should become feasible with the launch of next-generation space missions (e.g., the James Webb Space Telescope or the Nancy Grace Roman Space Telescope) that can provide photometric depth and angular resolution similar to those we have adopted when constructing our mock data sets.

On the other hand, while the binary separation function for foreground nonmembers within our mock data sets are motivated by recent observational results (Tian et al. 2019), at present, we have no way of knowing whether the binary fractions and separation functions adopted for the mock dSph member populations are realistic, optimistic, or even pessimistic regarding the number of detectable binary systems. Given this basic uncertainty, the properties of our mock dSph binary populations should not be interpreted as forecasts. Rather, our adoption of fixed binary fractions are intended, given the range of luminosities and distances within the population of Milky Way dSphs, merely to provide mock data sets containing a wide range of numbers of detectable binaries for testing our methodology. Reassuringly, we have found that when the number of detectable binaries approaches zero, our modeling accurately recovers that input; thus in the case that real dSphs contain few or no wide binaries that are detectable in future observations, we expect to be able to place limits on the underlying populations. Such limits can then be useful for constraining wide binary formation/evolution mechanisms and/or dark matter models.

Some additional caveats apply to the results from our analysis of mock data sets. While the mock data sets are intended to be realistic in terms of structural parameters and magnitude and resolution limits, they do have some idealized features that will not hold in real observational data sets. First, the mock dSph surface density functions are all circularly symmetric, whereas observed dSphs typically have ellipticities $0.1 \lesssim \epsilon \lesssim 0.5$ (McConnachie 2012, and references therein). In principle, our analysis need not assume circular symmetry, as the separation functions in Equations (1)–(3) hold for arbitrary surface density functions. In practice, relaxing the modeling assumption of circular symmetry may incur significant additional computational expense as the joint density $p(s, \mathbf{R})$ may no longer be expressed analytically.

Second, when generating the mock data sets, we have assumed that resolution and magnitude limits are independent. In reality, the minimum separation between two discernible point sources will depend on the magnitudes of both objects (e.g., Chauvin et al. 2004). In order to account for this dependence in real data, provided that it can be quantified using, e.g., artificial star tests, we can update our likelihood function (Equation (25)) to include this dependence directly (see, e.g., El-Badry & Rix 2018; Tian et al. 2019). We reserve this task for future work, where we plan to test our methodology on more realistic observational catalogs derived from mock images.

Third, we reiterate that the approximate likelihood in Equation (25) neglects observational errors associated with measurements of stellar position, as well as covariance among the nonindependent discrete data points in the data vector. Comparison of the resulting posteriors to the true input values gives some reassurance that the errors introduced by this approximation are not dramatic—at least not for the input models and mock data sets considered here; however, a more rigorous calculation of the likelihood will necessarily include

covariance. We leave this task for future work that focuses on modeling data from simulated images.

Finally, we note that the formalism presented in Section 2 has potential applications well beyond the analysis of binary star systems. For example, given a population of surface density $\Sigma(\mathbf{R})$, Equation (3) can be used to compute directly the probability of random pairings at a given separation, precluding the generation of “random” catalogs when estimating two-point correlation functions. Furthermore, one could then compare the empirical separation function to the “random” one predicted by Equation (3) in order to detect in separation space any unmodeled components of the surface density field—e.g., localized substructure and/or underdense regions.

We thank Andrew Pace for providing valuable advice and input. We thank Lachlan Lancaster, Eric Bell, Anil Seth, and Benjamin Williams for providing helpful feedback. M.G.W. acknowledges support from National Science Foundation grants AST-1813881 and AST-1909584, and from a grant from the McWilliams Center for Cosmology at Carnegie Mellon University and the Pittsburgh Supercomputing Center. Support for this work was provided in part by the WFIRST Infrared Nearby Galaxies Survey collaboration through NASA contract NNG16PJ28C. Based on observations with the NASA/ESA Hubble Space Telescope obtained from the Data Archive at the Space Telescope Science Institute, which is operated by the Association of Universities for Research in Astronomy, Incorporated, under NASA contract NAS5- 26555. Support for Program number HST-AR-16639.001-A and was provided through a grant from the STScI under NASA contract NAS5- 26555.

Appendix A

Derivation of Joint Position-separation Function

The joint position-separation function for countable items, $\psi'(s, \mathbf{R})$, can be written as the sum of contributions from all combinations of pairings between the different categories of countable items,

$$\psi'(s, \mathbf{R}) = \sum_m \sum_n \psi'_{m,n}(s, \mathbf{R}), \quad (\text{A1})$$

where categorical variables m, n both take values of “singles”, “primaries” from binary objects, and “secondaries” from binary objects. Contributions from pairings between primaries and secondaries depend on whether the two paired items belong to the same binary object. All pairings between items not belonging to the same binary object contribute as (see Equation (2))

$$\begin{aligned} \psi'_{m,n}(s, \mathbf{R}) &= \Sigma'_m(\mathbf{R}) \mu'_n(s|\mathbf{R}); \\ &\times m, n \text{ from different objects,} \end{aligned} \quad (\text{A2})$$

where $\Sigma'_m(\mathbf{R})$ is the surface number density of countable items in category m , and $\mu'_n(s|\mathbf{R}) \equiv \int_0^{2\pi} \Sigma'_n(\mathbf{R} + \Delta\mathbf{R})s d\alpha$ is the conditional separation function for countable items from category n . Pairings between primaries and secondaries from the same binary object contribute as

$$\psi'_{m,n}(s, \mathbf{R}) = \Sigma'_m(\mathbf{R}) \phi_b(s|\mathbf{R}); \quad m, n \text{ from same object,} \quad (\text{A3})$$

where $\phi_b(s|\mathbf{R})$ is the internal separation function for the binary pairs, normalized to $\int \phi_b(s|\mathbf{R}) ds = 1$.

Table 2
Contributions to $\psi'(s, \mathbf{R})$ from All Possible Pair Combinations of Item Categories

m	n	$\psi'_{m,n}(s, \mathbf{R})$
single	single	$(1 - f_b(\mathbf{R}))^2 \psi(s, \mathbf{R})$
single	primary	$\approx (1 - f_b(\mathbf{R})) f_b(\mathbf{R}) \psi(s, \mathbf{R})$
single	secondary	$\approx (1 - f_b(\mathbf{R})) f_b(\mathbf{R}) \psi(s, \mathbf{R})$
primary	single	$\approx (1 - f_b(\mathbf{R})) f_b(\mathbf{R}) \psi(s, \mathbf{R})$
primary	primary	$\approx (f_b(\mathbf{R}))^2 \psi(s, \mathbf{R})$
primary	secondary—same object	$\approx f_b(\mathbf{R}) \Sigma(\mathbf{R}) \phi_b(s \mathbf{R})$
primary	secondary—different object	$\approx (f_b(\mathbf{R}))^2 \psi(s, \mathbf{R})$
secondary	single	$\approx (1 - f_b(\mathbf{R})) f_b(\mathbf{R}) \psi(s, \mathbf{R})$
secondary	primary— same object	$\approx f_b(\mathbf{R}) \Sigma(\mathbf{R}) \phi_b(s \mathbf{R})$
secondary	primary—different object	$\approx (f_b(\mathbf{R}))^2 \psi(s, \mathbf{R})$
secondary	secondary	$\approx (f_b(\mathbf{R}))^2 \psi(s, \mathbf{R})$

The surface number density of “single” countable items is $\Sigma'_{\text{singles}}(\mathbf{R}) = (1 - f_b(\mathbf{R})) \Sigma(\mathbf{R})$, where $\Sigma(\mathbf{R})$ is the surface number density of statistically independent objects (a binary system is one object containing two countable items). The surface number densities of both “primary” and “secondary” countable items are approximately (see below) $\Sigma'_{\text{pri}}(\mathbf{R}) \approx \Sigma'_{\text{sec}}(\mathbf{R}) \approx f_b(\mathbf{R}) \Sigma(\mathbf{R})$. Likewise, the conditional separation functions of singles, primaries, and secondaries are $\mu'_{\text{singles}}(s|\mathbf{R}) = (1 - f_b(\mathbf{R})) \mu(s|\mathbf{R})$ and $\mu'_{\text{pri}}(s|\mathbf{R}) \approx \mu'_{\text{sec}}(s|\mathbf{R}) \approx f_b(\mathbf{R}) \mu(s|\mathbf{R})$. These approximations are valid as long as the binary separations are small compared to the scale over which the surface density changes.⁶

Table 2 lists the contribution to $\psi'(s, \mathbf{R})$ from each possible combination of categorical pairs. The sum is (Equation (7))

$$\psi'(s, \mathbf{R}) \approx (1 + f_b(\mathbf{R}))^2 \psi(s, \mathbf{R}) + 2f_b(\mathbf{R}) \Sigma(\mathbf{R}) \phi_b(s|\mathbf{R}). \quad (\text{A4})$$

ORCID iDs

Christopher Kervick  <https://orcid.org/0000-0001-5781-0598>
Matthew G. Walker  <https://orcid.org/0000-0003-2496-1925>
Sergey E. Koposov  <https://orcid.org/0000-0003-2644-135X>

References

- Andrews, J. J., Chanamé, J., & Agüeros, M. A. 2017, *MNRAS*, 472, 675
Baddeley, A., Rubak, E., & Turner, R. 2016, *Spatial Point Patterns* (Boca Raton, FL: CRC Press)
Bahcall, J. N., Hut, P., & Tremaine, S. 1985, *ApJ*, 290, 15
Bressan, A., Marigo, P., Girardi, L., et al. 2012, *MNRAS*, 427, 127
Buchner, J., Georgakakis, A., Nandra, K., et al. 2014, *A&A*, 564, A125
Chanamé, J., & Gould, A. 2004, *ApJ*, 601, 289
Chandrasekhar, S. 1944, *ApJ*, 99, 54
Chauvin, G., Lagrange, A. M., Dumas, C., et al. 2004, *A&A*, 425, L29
Davis, M., & Peebles, P. J. E. 1983, *ApJ*, 267, 465
DES Collaboration, Abbott, T. M. C., Aguena, M., et al. 2022, *PhRvD*, 105, 023520
Drlica-Wagner, A., Bechtol, K., Rykoff, E., et al. 2015, *ApJ*, 813, 109
Duquenooy, A., & Mayor, M. 1991, *A&A*, 248, 485
El-Badry, K., & Rix, H.-W. 2018, *MNRAS*, 480, 4884
Feroz, F., Hobson, M., & Bridges, M. 2009, *MNRAS*, 398, 1601
Feroz, F., & Hobson, M. P. 2008, *MNRAS*, 384, 449

⁶ Letting \mathbf{R} and $\mathbf{R} + \Delta\mathbf{R}$ denote the positions of primaries and secondaries, respectively, and considering all the binary pairs generated for dSph members in the mock data sets used in this work (Section 3.1), the mean fractional error introduced by this approximation is $(\Sigma(\mathbf{R} + \Delta\mathbf{R}) - \Sigma(\mathbf{R})) / \Sigma(\mathbf{R}) \approx 5 \times 10^{-5}$.

- Gaia Collaboration, Brown, A. G. A., Vallenari, A., et al. 2021, *A&A*, 649, A1
- Geha, M., Brown, T. M., Tumlinson, J., et al. 2013, *ApJ*, 771, 29
- Hamilton, A. J. S. 1993, *ApJ*, 417, 19
- Hammersley, J. M. 1950, *Ann. Math. Stat.*, 21, 447
- Heggie, D. C. 1975, *MNRAS*, 173, 729
- Hernandez, X., & Lee, W. H. 2008, *MNRAS*, 387, 1727
- Irwin, M., & Hatzidimitriou, D. 1995, *MNRAS*, 277, 1354
- Jiang, Y.-F., & Tremaine, S. 2010, *MNRAS*, 401, 977
- Koch, A., Hansen, T., Feltzing, S., & Wilkinson, M. I. 2014, *ApJ*, 780, 91
- Koposov, S. E., Belokurov, V., Torrealba, G., & Evans, N. W. 2015, *ApJ*, 805, 130
- Koposov, S. E., Gilmore, G., Walker, M. G., et al. 2011, *ApJ*, 736, 146
- Kouwenhoven, M. B. N., Brown, A. G. A., Portegies Zwart, S. F., & Kaper, L. 2007, *A&A*, 474, 77
- Kouwenhoven, M. B. N., Goodwin, S. P., Parker, R. J., et al. 2010, *MNRAS*, 404, 1835
- Kraus, A. L., & Hillenbrand, L. A. 2008, *ApJL*, 686, L111
- Kroupa, P. 2001, *MNRAS*, 322, 231
- Kroupa, P. 2002, *Sci*, 295, 82
- Landy, S. D., & Szalay, A. S. 1993, *ApJ*, 412, 64
- Lellouche, S., & Souris, M. 2020, *Stats*, 3, 1
- Lépine, S., & Bongiorno, B. 2007, *AJ*, 133, 889
- Longhitano, M., & Binggeli, B. 2010, *A&A*, 509, A46
- Martin, N. F., de Jong, J. T. A., & Rix, H.-W. 2008, *ApJ*, 684, 1075
- Martinez, G. D., Minor, Q. E., Bullock, J., et al. 2011, *ApJ*, 738, 55
- Mateo, M. L. 1998, *ARA&A*, 36, 435
- McConnachie, A. W. 2012, *AJ*, 144, 4
- Minor, Q. E. 2013, *ApJ*, 779, 116
- Moeckel, N., & Bate, M. R. 2010, *MNRAS*, 404, 721
- Moeckel, N., & Clarke, C. J. 2011, *MNRAS*, 415, 1179
- Moskowitz, A., & Walker, M. 2020, *ApJ*, 892, 27
- Öpik, E. 1924, *PTarO*, 25, 1
- Peebles, P. J. E. 1980, *The Large-scale Structure of the Universe* (Princeton, NJ: Princeton Univ. Press)
- Peñarrubia, J. 2021, *MNRAS*, 501, 3670
- Peñarrubia, J., Koposov, S. E., Walker, M. G., et al. 2010, arXiv:1005.5388
- Peñarrubia, J., Ludlow, A. D., Chanamé, J., & Walker, M. G. 2016, *MNRAS*, 461, L72
- Plummer, H. C. 1911, *MNRAS*, 71, 460
- Raghavan, D., McAlister, H. A., Henry, T. J., et al. 2010, *ApJS*, 190, 1
- Reipurth, B., & Mikkola, S. 2012, *Natur*, 492, 221
- Richardson, J. C., Irwin, M. J., McConnachie, A. W., et al. 2011, *ApJ*, 732, 76
- Simon, J. D. 2019, *ARA&A*, 57, 375
- Skilling, J. 2004, in *AIP Conf. Ser.*, 735, *Bayesian Inference and Maximum Entropy Methods in Science and Engineering: 24th Int. Workshop on Bayesian Inference and Maximum Entropy Methods in Science and Engineering*, ed. R. Fischer, R. Preuss, & U. V. Toussaint (Melville, NY: AIP), 395
- Spencer, M. E., Mateo, M., Olszewski, E. W., et al. 2018, *AJ*, 156, 257
- Springel, V., Wang, J., Vogelsberger, M., et al. 2008, *MNRAS*, 391, 1685
- Tian, H.-J., El-Badry, K., Rix, H.-W., & Gould, A. 2019, *ApJS*, 246, 4
- Tokovinin, A. 2017, *MNRAS*, 468, 3461
- Weinberg, M. D., Shapiro, S. L., & Wasserman, I. 1987, *ApJ*, 312, 367
- Yoo, J., Chanamé, J., & Gould, A. 2004, *ApJ*, 601, 311